SOLAR CELLS

Improved charge extraction in inverted perovskite solar cells with dual-site-binding ligands

Hao Chen[1,2]†, Cheng Liu[1]†, Jian Xu[2]†, Aidan Maxwell[2]†, Wei Zhou[3]†, Yi Yang[1], Qilin Zhou[3], Abdulaziz S. R. Bati[1], Haoyue Wan[2], Zaiwei Wang[2], Lewei Zeng[2], Junke Wang[2], Peter Serles[4], Yuan Liu[1], Sam Teale[2], Yanjiang Liu[2], Makhsud I. Saidaminov[5], Muzhi Li[6], Nicholas Rolston[6], Sjoerd Hoogland[2], Tobin Filleter[4], Mercouri G. Kanatzidis[1], Bin Chen[1]*, Zhijun Ning[3]*, Edward H. Sargent[1,2,7]*

Inverted (pin) perovskite solar cells (PSCs) afford improved operating stability in comparison to their nip counterparts but have lagged in power conversion efficiency (PCE). The energetic losses responsible for this PCE deficit in pin PSCs occur primarily at the interfaces between the perovskite and the charge-transport layers. Additive and surface treatments that use passivating ligands usually bind to a single active binding site: This dense packing of electrically resistive passivants perpendicular to the surface may limit the fill factor in pin PSCs. We identified ligands that bind two neighboring lead(II) ion (Pb^{2+}) defect sites in a planar ligand orientation on the perovskite. We fabricated pin PSCs and report a certified quasi–steady state PCE of 26.15 and 24.74% for 0.05– and 1.04–square centimeter illuminated areas, respectively. The devices retain 95% of their initial PCE after 1200 hours of continuous 1 sun maximum power point operation at 65°C.

The certified power conversion efficiency (PCE) of perovskite solar cells (PSCs) has reached an impressive 25.7% (*1*). Nevertheless, the most-efficient PSCs, fabricated in the nip architecture, have yet to achieve the needed operating stability under accelerated aging tests (*1, 2*). Inverted (pin) PSCs, which do not rely on p-type dopants in their hole-transporting layers (*3–7*), have seen progress but, until now, still lag behind their nip counterparts: Their stabilized PCE has so far reached only 25.1% (*8*). The interfaces between the perovskite and the charge-transport layers limit the PCE of pin cells (*9–11*) through band misalignment (*12*) and energy-level pinning (*11*). These problems are aggravated by the presence of surface defects. For example, undercoordinated Pb^{2+} ions (*13–15*) result in nonradiative recombination at the perovskite–charge transport layer interface, which limits photovoltage and fill factor (FF).

Surface passivation of the perovskite active layer is used to suppress interface nonradiative recombination (*14, 16*). The efficacy of bulk additives as well as solution-based treatments with ammonium ligands is now well estab-

lished (*17, 18*). However, these ligands bind at a single active binding site to the perovskite structure, and this has the potential to produce dense packing of passivants aligned perpendicular to the surface, introducing an unwanted resistive barrier between the perovskite and the electron transport layer (ETL) (*16, 19–25*). We sought routes to passivate undercoordinated Pb^{2+} at the surfaces and grain boundaries of the perovskite with passivator ligands aligning parallel to the perovskite surface instead.

Theoretical investigations

We began by considering candidate molecules that contain a benzene ring because its flat structure is expected to lie parallel to a surface compared with the case of linear-chain ligands (*21*). To enable strong binding with perovskite surfaces, we considered both $-PO_3^{2-}$ and $-SO_3^-$ functional groups, each of which is reported to coordinate strongly with Pb^{2+} (*14, 26*). Because benzenephosphonates are not readily available, we focused on available sulfonates (*27–33*). We prioritized end functional groups that have a high number of oxygen atoms, a feature recently reported to correlate positively with strong binding (*26*).

We then evaluated steric constraints, seeking a ligand sufficiently long that it could bind at multiple surface Pb sites, these being ~6.3 Å apart in the case of formamidinium (FA)–based perovskites. These considerations pointed to benzenesulfonate (BZS) ligands and their derivatives because these molecules have a length of ~5.7 Å.

We used density functional theory (DFT) calculations to investigate how the molecular structure of the ligand affects orientation. We considered three ligands, one with no additional functional group (BZS) and two with

methyl or chloride in the para position of benzene ring opposite to the sulfonate functional group [4-methylbenzenesulfonate (4CH$_3$-BZS) and 4-chlorobenzenesulfonate (4Cl-BZS)] (Fig. 1A). 4CH$_3$-BZS and 4Cl-BZS have lengths of 6.14 and 6.37 Å, respectively. We compared the formation energies of two configurations, one in which the ligands were oriented perpendicular to the perovskite surface (Conf-perp; Fig. 1B) and another in which the ligands adopted a parallel orientation with respect to the perovskite surface (Conf-para; Fig. 1C). Although Conf-perp was more energetically favorable for BZS and 4CH$_3$-BZS, Conf-para was energetically more favorable for 4Cl-BZS because of the additional Pb^{2+} surface binding afforded by the Cl functional group (Fig. 1D) that would enable dual-site Pb^{2+} passivation. We also investigated the effects of ligand orientation on charge transfer at the perovskite-ETL interface by examining fullerene (C_{60}), which is widely used as an ETL in pin PSCs and is known to induce energetic losses in devices (*11, 12, 34, 35*). Analysis of the calculated charge density difference (Fig. 1E and fig. S1) provided evidence that 4Cl-BZS, when absorbed on the perovskite layer, established a notably stronger binding strength with the C_{60} layer [adsorption energies (E_{ads}) = −0.85 eV] in contrast to BZS (E_{ads} = −0.46 eV) and 4CH$_3$-BZS (E_{ads} = −0.39 eV) (*36*). Fracture energy (G_c) results show that 4Cl-BZS increases the mechanical strength of the perovskite-C_{60} interface (fig. S2) (*37*).

Ligand-perovskite binding characterization

To explore interactions between perovskite and BZS ligands, we began by adding each ligand directly into the precursor solutions and spin-coating $Cs_{0.05}FA_{0.85}MA_{0.1}PbI_3$ perovskite thin films, where FA is formamidinium and MA is methylamine. Time-of-flight secondary ion mass spectrometry (TOF-SIMS) of untreated (control) and treated films showed that BZS, 4CH$_3$-BZS, and 4Cl-BZS were all concentrated near the top (ETL-facing) surface of the perovskite film (fig. S3). This result, combined with x-ray diffraction (XRD) patterns of control and treated perovskite films that showed no discernable peak-shifting after treatment (fig. S4), indicated that the ligands did not enter the lattice but rather diffused toward the top surface during film crystallization. Scanning electron microscopy (SEM) images of perovskite films with additives are presented in fig. S5 and illustrate that the perovskite films (both additives and controls) exhibit substantially uniform morphology.

We used x-ray photoelectron spectroscopy (XPS) to check for possible evidence of interaction between the additives and perovskite. We observed a shift of the Pb 4*f* XPS peaks to a lower binding energy for each treated film compared with the peaks of controls (Fig. 2A).

[1]Department of Chemistry, Northwestern University, Evanston, IL 60208, USA. [2]Department of Electrical and Computer Engineering, University of Toronto, Toronto, ON M5S 1A4, Canada. [3]School of Physical Science and Technology, ShanghaiTech University, Shanghai, China. [4]Department of Mechanical and Industrial Engineering, University of Toronto, Toronto, ON M5S 3G8, Canada. [5]Department of Electrical and Computer Engineering, University of Victoria, Victoria, BC V8P 5C2, Canada. [6]Ira A. Fulton Schools of Engineering, Arizona State University, Tempe, AZ 85281, USA. [7]Department of Electrical and Computer Engineering, Northwestern University, Evanston, IL 60208, USA.
*Corresponding author. Email: bin.chen@northwestern.edu (B.C.); ningzhj@shanghaitech.edu.cn (Z.N.); ted.sargent@northwestern.edu (E.H.S.)
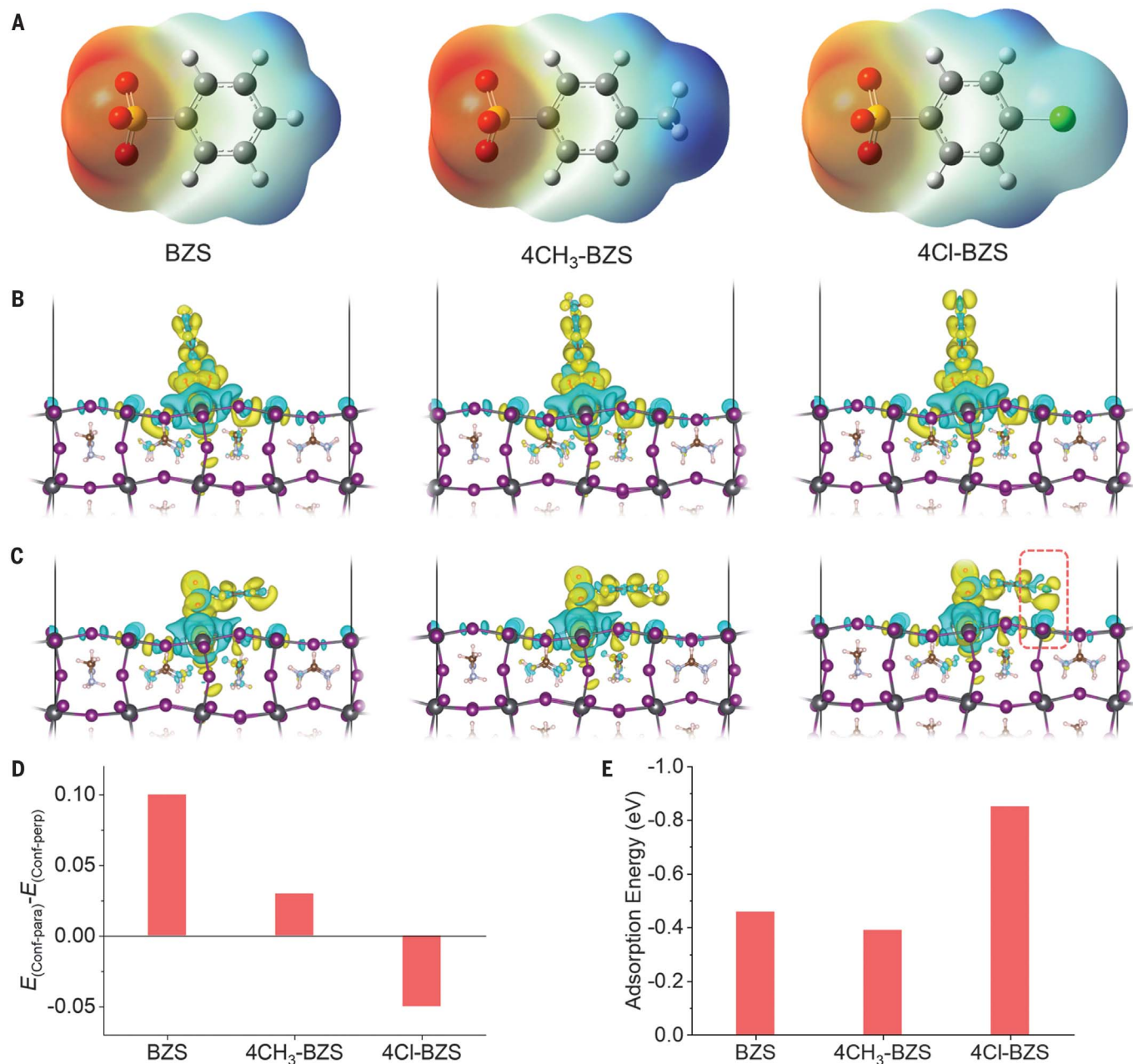†These authors contributed equally to this work.

Fig. 1. DFT studies of ligand binding and predicted orientation. (**A**) Structure and electrostatic potential of BZS, 4CH$_3$-BZS, and 4Cl-BZS ligands. (**B**) Atomic structures of ligand adsorbed in a perpendicular orientation (Conf-perp) on the perovskite surface. (**C**) Atomic structures of ligand adsorbed in a planar or parallel orientation (Conf-para) on the perovskite surface. (**D**) Formation energy difference between parallel and perpendicular ligand-surface orientations ($E_{Conf-para} - E_{Conf-perp}$). (**E**) The adsorption energies (E_{ads}) of C$_{60}$ with different molecules (BZS, 4CH$_3$-BZS, and 4Cl-BZS) adsorbed on the perovskite surface.

We saw evidence of interaction between Cl and Pb in 4Cl-BZS–treated perovskite from both XPS spectra (Fig. 2B) and nuclear magnetic resonance spectra (fig. S6).

Optoelectronic characterization of perovskite films and device stacks

To evaluate the passivation efficacy of each ligand, we studied photoluminescence (PL) of neat control and treated perovskite films.

We observed an increase in PL quantum yield (PLQY) for each of the treated films and the full device stack (Fig. 2C), with 4Cl-BZS exhibiting a twofold increase in PLQY (41%) compared with control films (20%), which corresponded to a projected 20-mV increase in quasi-Fermi level splitting (QFLS). The PLQY of full-device stacks [FTO/SAMs/perovskite/C$_{60}$, where FTO is fluorinate tin oxide and SAMs (self-assembled monolayers) are mixtures of 2PACz and Me-4PACz] revealed a substantial improvement after 4Cl-BZS treatment—5% for 4Cl-BZS compared with 0.6% for the control, corresponding to 1.17 and 1.1 V in QFLS for 4Cl-BZS and the control device, respectively. This improvement was consistent with reduced interface losses. Time-resolved photoluminescence (TRPL) revealed a similar increase in carrier lifetimes after treatment. Specifically, 4Cl-BZS–treated films exhibited a weighted-average lifetime of
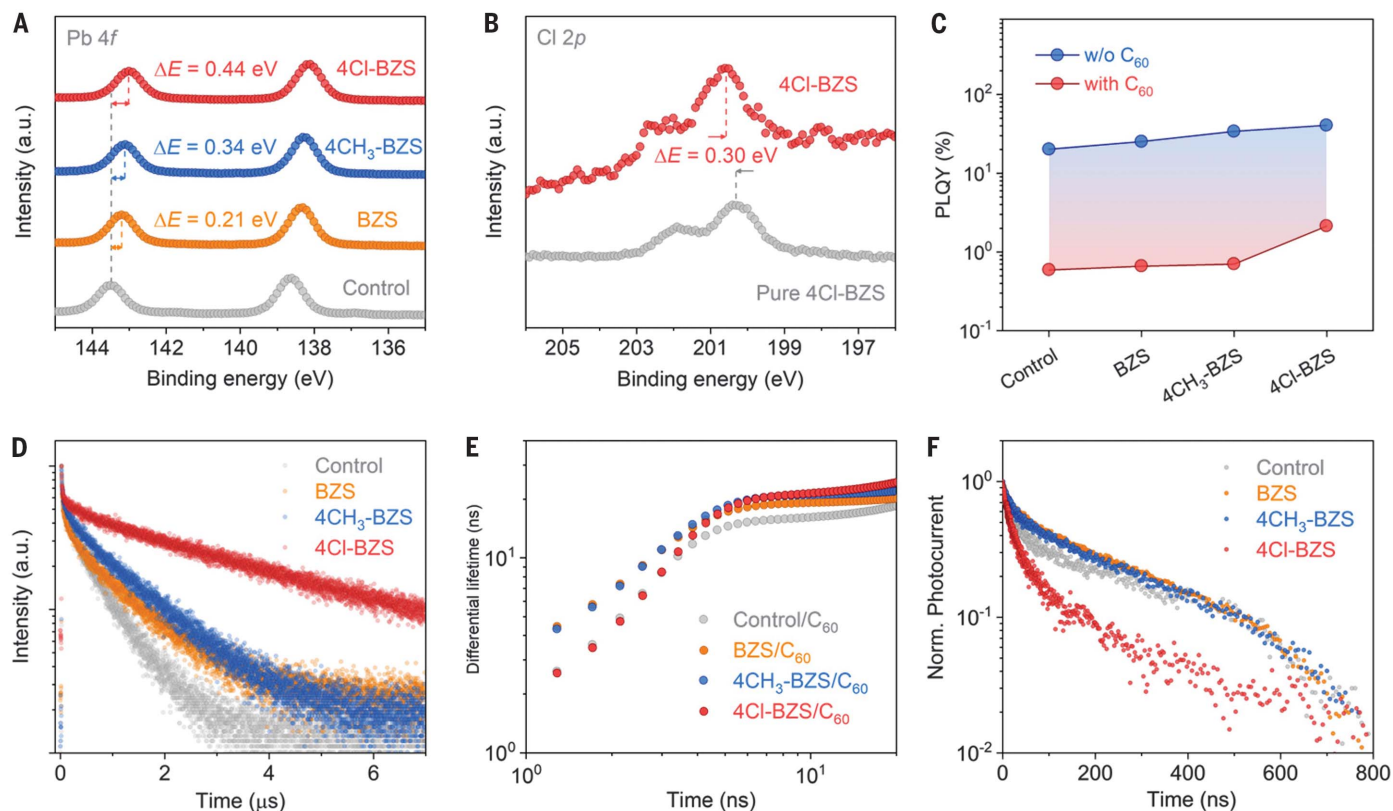
Fig. 2. Surface coordination and passivation of perovskite films. (**A**) Pb 4f XPS spectra of control and treated perovskite surfaces. a.u., arbitrary units. (**B**) Cl 2p XPS spectra of pure 4Cl-BZS film compared with spectra of perovskite treated with 4Cl-BZS. (**C**) PLQY of neat control and treated perovskite films on quartz substrates and PLQY results for full device stacks (FTO/SAMs/ perovskite/C_{60}) with and without treatment. (**D**) TRPL lifetimes of neat control and treated perovskite films. The lifetimes for each trace were calculated using a biexponential decay model and can be found in table S1. (**E**) Differential carrier lifetimes extracted from the TRPL spectrum (fig. S7). (**F**) Transient photocurrent (TPC) measurements of control and treated devices.

3.0 μs compared with 0.6 μs for the control film (Fig. 2D and table S1).

We fabricated partial and full perovskite/ ETL device stacks to probe interface recombination and charge transfer. First, we conducted TRPL measurements of perovskite/C_{60} stacks, wherein decay was dictated by nonradiative surface-bulk recombination (monoexponential decay), radiative recombination (second-order decay), and charge extraction effects, which could be distinguished if the time constants for each process differed sufficiently (38). The first interval at shorter times was dominated by the transfer of electrons from the bulk into the C_{60}, and the second interval at longer delay times was dominated by interfacial recombination (39). The sharp drop in emission for 4Cl-BZS/C_{60} indicated efficient electron transfer at the interface, and the longer second-order decay time was indicative of a reduced trap density compared with BZS and 4CH₃-BZS (fig. S7). This effect of this reduction was especially evident in fits to the TRPL traces to compute the differential lifetime as $\tau = -\{d \ln[\phi(t)]/dt\}^{-1}$ (Fig. 2E), where $\phi(t)$ is the time-dependent PL photon flux, because

the sharpness of the rise implied the speed of the electron transfer from perovskite to C_{60}.

Transient photocurrent measurements of full device stacks in which we used mixed SAMs as the hole-transport layer (see methods) revealed a similar trend. Both BZS and 4CH₃-BZS resulted in slower photocurrent decay, whereas 4Cl-BZS treatment led to faster photocurrent decay (Fig. 2F). This observation suggested that electron extraction became more efficient. Ultraviolet photoelectron spectroscopy (UPS) revealed an increased conduction band offset with C_{60} that was caused by a Fermi-level upshift after BZS and 4CH₃-BZS treatment, whereas 4Cl-BZS caused a Fermi-level downshift and reduced conduction band offset (figs. S8 and S9). This trend was further confirmed by kelvin probe force microscopy (KPFM) measurements (fig. S10 and table S2) and DFT calculations (fig. S11).

Inverted perovskite solar cells

Using 4Cl-BZS–treated perovskite, we fabricated inverted PSCs with the structure FTO/SAMs/ perovskite/C_{60}/SnO$_x$/Ag (Fig. 3A). The thickness of the perovskite layer was 900 nm. Con-

trol devices had a PCE of 24%, whereas the 4Cl-BZS–treated devices exhibited a PCE of 26.3% (fig. S12). Analysis of device statistics for both control and 4Cl-BZS–treated PSCs revealed a substantial enhancement in PCE, primarily by increased open-circuit voltage (V_{OC}). Additionally, 4Cl-BZS–treated PSCs showed a much higher FF compared with BZS- and 4CH₃-BZS–treated PSCs. We attribute this improvement in FF to enhanced charge extraction in 4Cl-BZS–treated PSCs (Fig. 3B and figs. S13 and S14).

We also evaluated the effectiveness of the additive change with a stronger or weaker donating group, namely 4F-BZS, 4Br-BZS, and 4I-BZS. Notably, 4F-BZS exhibits a more-negative averaged electrostatic potential, whereas 4I-BZS displays a more-positive averaged electrostatic potential (fig. S15). We posit that a stronger donating group, such as Cl or F, is beneficial in providing dual-site defect passivation. Because 4F-BZS, 4Cl-BZS, and 4I-BZS are not readily available, we used the structurally similar molecules 4-fluorobenzenesufonic acid (4F-BZSA) and 4-iodobenzenesufonic acid (4I-BZSA) in our devices (fig. S16). Notably, treatments with 4F-BZSA resulted in comparable PCE as in the
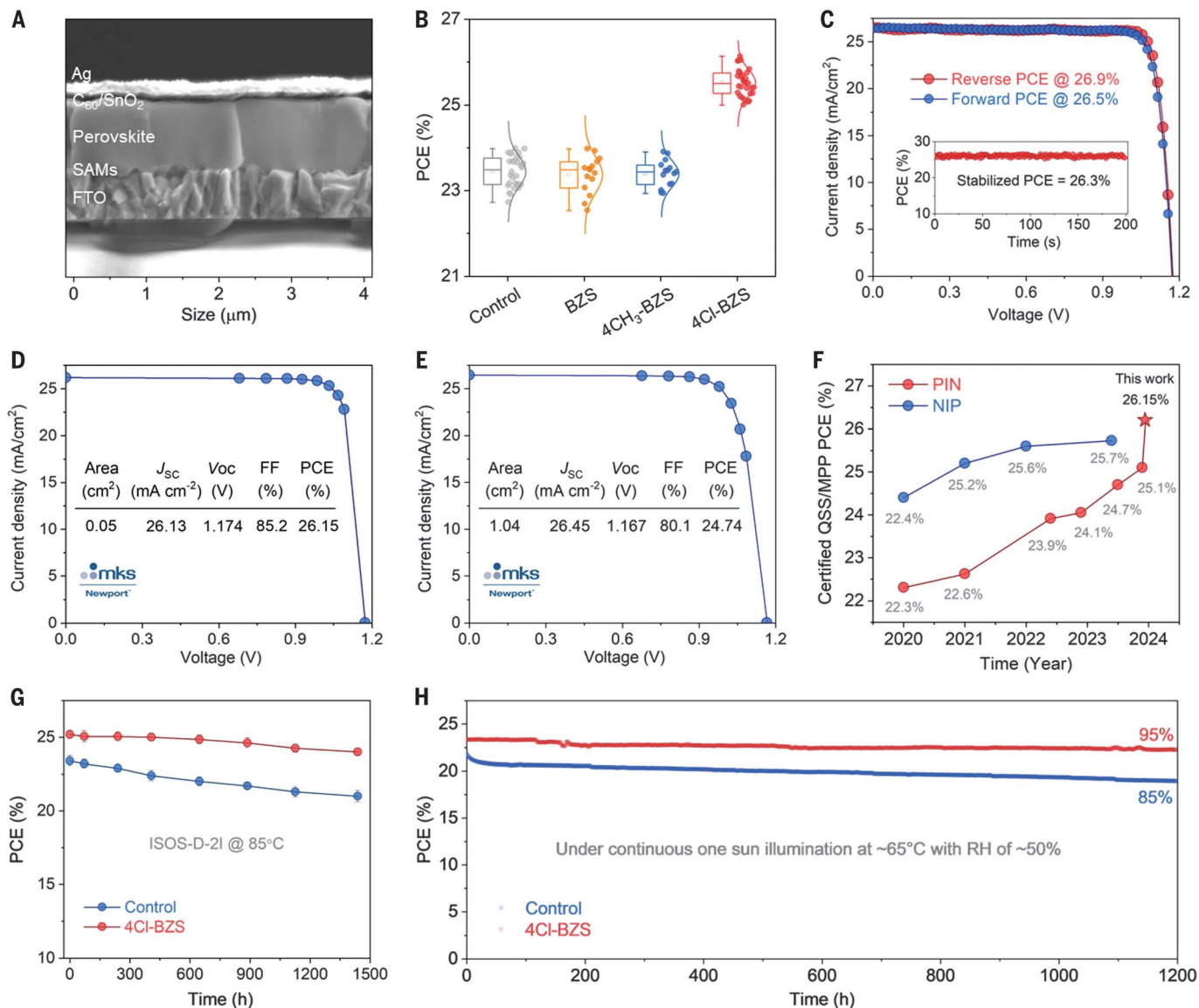
Fig. 3. Photovoltaic performance and stability of inverted solar cells.
(**A**) Cross-sectional SEM image of the device structure. (**B**) PCE statistics for
30 control and 4Cl-BZS–treated devices. The center line represents the median,
box limits are upper and lower quartiles, and whiskers are minimum and
maximum values; the vertical curved lines represent data distribution. (**C**) J-V
curves of the 4Cl-BZS–treated device with bimolecular passivation. The inset
shows the stabilized PCE. (**D**) Newport-certified QSS J-V curve of the champion
0.05-cm² device (fig. S15). (**E**) Newport-certified QSS J-V curve of the champion
1.04-cm² device (fig. S16). (**F**) Summary of published nip and pin PSC
performances in recent years. (**G**) ISOS-D-2I device stability during storage
at 85°C for 1500 hours. (**H**) MPP stability tracking of encapsulated control and
4Cl-BZS–treated devices under simulated 1-sun illumination at 50% relative
humidity (RH) and a heatsink temperature of 65°C. The 4Cl-BZS–treated device
retains 95% of its initial efficiency after 1200 hours of operation.

case of 4Cl-BZS, and 4I-BZSA also showed an
improved PCE compared with controls.

We then added the bimolecular surface pas-
sivation (BMP) approach, based on 3-(methylthio)
propylamine hydroiodide (3MTPAI) and propane-
1,3 diammonium iodide (PDAI₂), reported in (8).
This strategy has been reported to provide a
combination of chemical and field-effect passi-
vation (see methods). The PLQY of full-device
stacks (FTO/SAMs/perovskite/BMP/C₆₀) indi-
cated a further improvement after the BMP
treatment (fig. S17). The combined treatment

increased the PCE of 4Cl-BZS–treated devices
from 26.3 to 26.9% and featured a V_{OC} of 1.18 V,
FF of 86.2%, and short-circuit current density
(J_{SC}) of 26.4 mA cm⁻² (Fig. 3C). Statistics of
photovoltaic parameters for devices with bi-
molecular passivation revealed additional im-
provements in both V_{OC} and PCE (fig. S18).

The bandgap of the pin PSCs was taken from
external quantum efficiency measurements
as 1.53 eV (figs. S19 and S20). We sent devices
with active areas of 0.05 and 1.04 cm² to a Na-
tional Renewable Energy Laboratory (NREL)–

accredited independent photovoltaic calibra-
tion laboratory (Newport) for certification. The
devices achieved certified stabilized quasi–
steady state (QSS) PCEs of 26.15 and 24.74%,
respectively (Fig. 3, D and E, and figs. S21 and
S22). These reported pin PSC PCEs surpass the
record nip device performance reported in re-
cent years (Fig. 3E and tables S3 and S4).

Next, we sought to test the thermal stability
of the 4Cl-BZS–treated PSCs following proto-
cols established by the International Sum-
mit on Organic Photovoltaic Stability (ISOS)

protocol ISOS-D-2I, in which encapsulated devices were subjected to dark storage at 85°C and tested periodically. 4Cl-BZS–treated PSCs retained 95% of their initial efficiency after 1500 hours of storage at 85°C (Fig. 3G). To evaluate operating stability further, we then also carried out ISOS-L-3 testing, in which encapsulated devices were subjected to continuous 1-sun equivalent illumination using a ultraviolet-free white light-emitting diode (LED) and held at the maximum power point (MPP) voltage, at 50% relative humidity and a heatsink temperature of 65°C (Fig. 3H). 4Cl-BZS–treated PSCs achieved a T_{95} (the time it takes for the device's PCE to drop to 95% of the initial value) of 1200 hours after continuous MPP tracking at 65°C, whereas control devices dropped from an initial efficiency of 22 to 18.7% after 1200 hours (table S5). Furthermore, 4Cl-BZS–treated PSCs achieved a T_{87} of 540 hours after continuous MPP tracking at 85°C (fig. 23).

Discussion

We began this study with the view that dense packing of passivator ligands perpendicular to the perovskite-C_{60} interface may increase resistance and that this could potentially be addressed by instead introducing ligands prone to align in a planar orientation relative to the perovskite surface. The interaction of 4Cl-BZS with undercoordinated Pb^{2+} ions reduces the surface defect density and minimizes the energetic mismatch between the perovskite and C_{60}. Our study indicates that the approach was effective in increasing pin PSC performance, bringing it into the range of that achieved in the nip configuration. Our approach retains the benefits of the 65°C 1-sun MPP operating stability seen in pin PSCs.

To test whether our approach worked in a range of perovskite compositions, we fabricated 4Cl-BZS–treated 1.78-eV wide-bandgap mixed halide devices as well as 1.25-eV narrow-bandgap mixed Pb-Sn PSCs, which are compositions of interest in all-perovskite tandem solar cells. In each case, we observed an increase in PCE after 4Cl-BZS treatment (fig. S24).

REFERENCES AND NOTES

1. J. Park et al., Nature 616, 724–730 (2023).
2. Y. Zhao et al., Science 377, 531–534 (2022).
3. H. Chen et al., Adv. Mater. 31, 1903559 (2019).
4. B. Chen et al., Adv. Mater. 33, e2103394 (2021).
5. Q. Jiang et al., Nature 611, 278–283 (2022).
6. S. You et al., Science 379, 288–294 (2023).
7. S. M. Park et al., Nature 624, 289–294 (2023).
8. C. Liu et al., Science 382, 810–815 (2023).
9. S. Cacovich et al., Nat. Commun. 13, 2868 (2022).
10. M. Stolterfoht et al., Nat. Energy 3, 847–854 (2018).
11. J. Warby et al., Adv. Energy Mater. 12, 2103567 (2022).
12. M. Stolterfoht et al., Energy Environ. Sci. 12, 2778–2788 (2019).
13. X. Gu, W. Xiang, Q. Tian, S. F. Liu, Angew. Chem. Int. Ed. 60, 23164–23170 (2021).
14. C. Li et al., Science 379, 690–694 (2023).
15. T. Yang et al., Nat. Commun. 14, 839 (2023).
16. S. M. Park et al., Science 381, 209–215 (2023).
17. F. Gao, Y. Zhao, X. Zhang, J. You, Adv. Energy Mater. 10, 1902650 (2020).
18. J. Xia et al., Energy Environ. Mater. 6, e12296 (2023).
19. M. G. La-Placa et al., ACS Energy Lett. 4, 2893–2901 (2019).
20. S. M. Park, A. Abtahi, A. M. Boehm, K. R. Graham, ACS Energy Lett. 5, 799–806 (2020).
21. H. Chen et al., Nat. Photonics 16, 352–358 (2022).
22. J. Chakkamalayath, N. Hiott, P. V. Kamat, ACS Energy Lett. 8, 169–171 (2023).
23. C. A. R. Perini et al., Adv. Mater. 34, e2204726 (2022).
24. K. Ma et al., Adv. Mater. 33, e2100791 (2021).
25. Q. Jiang et al., Nat. Photonics 13, 460–466 (2019).
26. J. Xu et al., Nat. Mater. 22, 1507–1514 (2023).
27. S. Kajal et al., Chem. Eng. J. 451, 138740 (2023).
28. Y. Hao et al., J. Mater. Chem. A Mater. Energy Sustain. 10, 13048–13054 (2022).
29. H. Wang et al., J. Mater. Chem. C Mater. Opt. Electron. Devices 11, 13518–13525 (2023).
30. R. Chen et al., J. Am. Chem. Soc. 143, 10624–10632 (2021).
31. K. Liu et al., Joule 4, 2404–2425 (2020).
32. J. C. Hamill Jr. et al., J. Phys. Chem. C Nanomater. Interfaces 124, 14496–14502 (2020).
33. K. Hills-Kimball, H. Yang, T. Cai, J. Wang, O. Chen, Adv. Sci. (Weinh.) 8, 2100214 (2021).
34. H. Chen et al., Nature 613, 676–681 (2023).
35. J. Liu et al., Science 377, 302–306 (2022).
36. B. Li et al., ACS Appl. Mater. Interfaces 10, 32471–32482 (2018).
37. M. Li et al., Energy Adv. 3, 273–280 (2024).
38. A. Al-Ashouri et al., Science 370, 1300–1309 (2020).
39. T. Li et al., Nat. Energy 8, 610–620 (2023).